Inorganic Chemistry

Article

Synthesis, Gas-Phase Photoelectron Spectroscopic, and Theoretical Studies of Stannylated Dinuclear Iron Dithiolates

Richard S. Glass,*,† Nadine E. Gruhn,† Edward Lorance,‡ Maya S. Singh,† Nhu Y T. Stessman,§ and Uzma I. Zakai†

Department of Chemistry, The University of Arizona, Tucson, Arizona 85721, and Department of Chemistry, Vanguard University, Costa Mesa, California 92626

Stannylated dinuclear iron dithiolates (μ-SSnMe$_2$CH$_2$S)[Fe(CO)$_3$]$_2$, (μ-SCH$_2$SnMe$_2$CH$_2$S) [Fe(CO)$_3$]$_2$, and (μ-SCH$_2$-SnMe$_3$)$_2$[Fe(CO)$_3$]$_2$, which are structurally similar to the active site of iron-only hydrogenase, were synthesized and studied by gas-phase photoelectron spectroscopy. The orbital origins of ionizations were assigned by comparison of He I and He II photoelectron spectra and with the aid of hybrid density functional electronic structure calculations. Stannylation lowers the ionization energy of sulfur lone pair orbitals in these systems owing to a geometry-dependent interaction. The Fe–Fe σ bond, which is the HOMO in all these systems, is also substantially destabilized by stannylation due to a previously unrecognized geometry-dependent interaction between axial sulfur lone pair orbitals and the Fe–Fe σ bond. Since cleaving the Fe–Fe σ bond is a key step in the mechanism of action of iron-only hydrogenase, these newly recognized geometry-dependent interactions may be utilized in designing biologically inspired hydrogenase catalysts.

Introduction

Hydrogenases[1] are a group of bacterial enzymes with a typically dinuclear active site that have attracted much interest lately for several reasons. The most common class of hydrogenase enzymes contains both Ni and Fe at the active site[2] as shown in **1**. In addition, Fe-only enzymes are known[3]

1

2
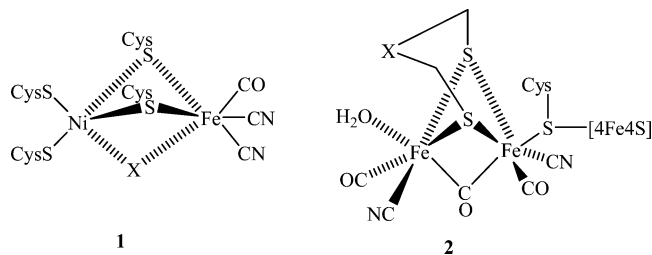
in which there are two Fe atoms at the active site as shown in **2**. Another class of hydrogenases found in Archaea has

also been reported. This class of hydrogenases utilizes a methenyltetrahydromethanopterin cofactor at a metal-free active site; however, it has recently been claimed[4] that this enzyme contains 1 mol of functional Fe. Remarkably, the active sites of the [Ni–Fe] and Fe-only hydrogenases contain both CO and CN$^-$ ligands. The biosynthetic origin of the CN$^-$ ligand is carbamoyl phosphate,[5] NH$_2$C(O)OPO$_3$H$^-$, and the unusual processing of carbamoyl phosphate to the $-$CN ligand has been elucidated.[6] Since these hydrogenase enzymes catalyze the production and uptake of dihydrogen, they are of interest as catalysts for both the production and consumption of H$_2$ in fuel cells.[7]

Chemical models for the active site of [Fe] H$_2$ase, such as **3a**–**c**, have been studied experimentally[8–10] and theoreti-

3a, X=CO
b, X=CN
c, X=Me$_3$P

4
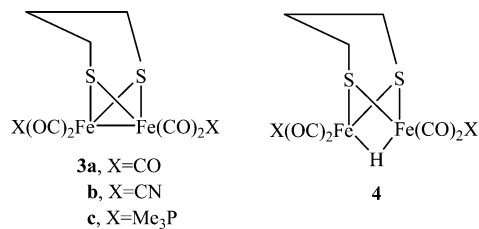
cally[11,12] to provide insight into the catalytic mechanism for the enzyme. Protonation of the Fe$-$Fe bond in **3** converts

* To whom correspondence should be addressed. E-mail: rglass@u.arizona.edu.
† University of Arizona.
‡ Vanguard University.
§ Current address: California State University, Stanislaus.

(1) Frey, M. *Struct. Bonding (Berlin)* **1998**, *90*, 97.
(2) Fontecilla-Camps, J. C.; Ragsdale, S. W. *Adv. Inorg. Chem.* **1999**, *47*, 283.
(3) Peters, J. W.; Lanzilotta, W. N.; Lemon, B. J.; Seefeldt, L. C. *Science* **1998**, *282*, 1853.

this formally Fe^I-Fe^I complex into $Fe^{II}(\mu\text{-H})Fe^{II}$ (**4**), which can then bind and heterolytically activate H_2. Protonation occurs for **3b** or **3c**, but not for **3a**, presumably because CN^- or PMe_3 are better donor ligands than CO, rendering the metal centers in both **3b** and **3c** more basic than that in **3a**. Could increasing the donor ability of the thiolate ligand in **3a** achieve the same effect as substituting a CO ligand with CN^- or PMe_3? Replacement of the central carbon with tin in the bridging dithiolate ligand of **3a** is anticipated to increase the electron density on sulfur without substantial structural changes. This paper reports the synthesis, gas-phase photoelectron spectroscopic, and theoretical studies of **5** and related compounds to explore the effect of stannylation upon these systems.

Results and Discussion

Stannylated dinuclear iron dithiolate **5** was synthesized by following literature precedent[13] for the synthesis of (μ-$SCH_2S)Fe_2(CO)_6$. Thus, reaction of the dithiol **6** with Me_2-$Sn(CH_2I)_2$[14] and Et_3N afforded **5**. Stannylated dinuclear iron

5   **6**
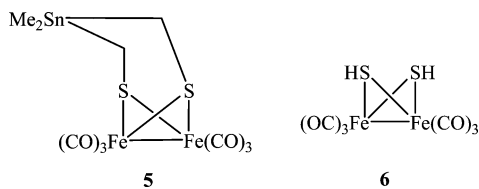
dithiolate **7** was prepared by first reducing disulfide **8**[15] with lithium triethylborohydride to give dithiolate **9**,[16] which was reacted with $Me_2Sn(I)CH_2I$[17] to provide **7** in 30% yield after isolation. The structure of **7** was unequivocally confirmed

(4) Lyon, E. J.; Shima, S.; Buurman, G.; Chowdhuri, S.; Batschauer, A.; Steinbach, H.; Thauer, R. K. *Eur. J. Biochem.* **2004**, *271*, 195.
(5) Paschos, A.; Glass, R. S.; Böck, A. *FEBS Lett.* **2001**, *488*, 9.
(6) Reissmann, S.; Hochleitner, E.; Wang, H.; Paschos, A.; Lottspeich, F.; Glass, R. S.; Böck, A. *Science* **2003**, *299*, 1067.
(7) *Hydrogen as Fuel*; Cammack, R., Frey, M., Robson, R., Eds.; Taylor and Francis: London, 2001.
(8) (a) Lyon, E. J.; Georgakaki, I. P.; Reibenspies, J. H.; Darensbourg, M. Y. *Angew. Chem., Int. Ed.* **1999**, *38*, 3178. (b) Zhao, X.; Georgakaki, I. P.; Miller, M. L.; Yarbrough, J. C.; Darensbourg, M. Y. *J. Am. Chem. Soc.* **2001**, *123*, 9710. (c) Zhao, X.; Georgakaki, I. P.; Miller, M. L.; Mejia-Rodriquez, R.; Chiang, C.-Y.; Darensbourg, M. Y. *Inorg. Chem.* **2002**, *41*, 3917. (d) Zhao, X.; Chiang, C.-Y.; Miller, M. L.; Rampersad, M. V.; Darensbourg, M. Y. *J. Am. Chem. Soc.* **2003**, *125*, 518. (e) Chong, D.; Georgakaki, I. P.; Mejia-Rodriguez, R.; Sanabria-Chinchilla, J.; Soriaga, M. P.; Darensbourg, M. Y. *Dalton Trans.* **2003**, 4158.
(9) (a) Schmidt, M.; Contakes, S. M.; Rauchfuss, T. B. *J. Am. Chem. Soc.* **1999**, *121*, 9736. (b) Gloaguen, F.; Lawrence, J. D.; Rauchfuss, T. B. *J. Am. Chem. Soc.* **2001**, *123*, 9476. (c) Gloaguen, F.; Lawrence, J. D.; Schmidt, M.; Wilson, S. R.; Rauchfuss, T. B. *J. Am. Chem. Soc.* **2001**, *123*, 12518.
(10) (a) Le Cloirec, A.; Best, S. P.; Borg, S.; Davies, S. C.; Evans, D. J.; Hughes, D. L.; Pickett, C. J. *Chem. Commun.* **1999**, 2285. (b) Tard, C.; Liu, X.; Ibrahim, S. K.; Bruschi, M.; DeGioia, L.; Davies, S. C.; Yang, X.; Wang, L. S.; Sawers, G.; Pickett, C. J. *Nature* **2005**, *433*, 610−613.
(11) Co, Z.; Hall, M. B. *J. Am. Chem. Soc.* **2001**, *123*, 3734.
(12) Bruschi, M.; Fantucci, P.; DeGioia, L. *Inorg. Chem.* **2002**, *41*, 1421.
(13) Seyferth, D.; Henderson, R. S. *J. Organomet. Chem.* **1981**, *218*, C34.
(14) Seyferth, D.; Andrews, S. B. *J. Organomet. Chem.* **1971**, *30*, 151.
(15) Brandt, P. F.; Lesch, D. A.; Stafford, P. R.; Rauchfuss, T. B. *Inorg. Synth.* **1997**, *31*, 112.
(16) (a) Seyferth, D.; Henderson, R. S.; Song, L. C. *J. Organomet. Chem.* **1980**, *192*, C1. (b) Seyferth, D., Henderson, R. S.; Song, L. C. *Organometallics* **1982**, *1*, 125.
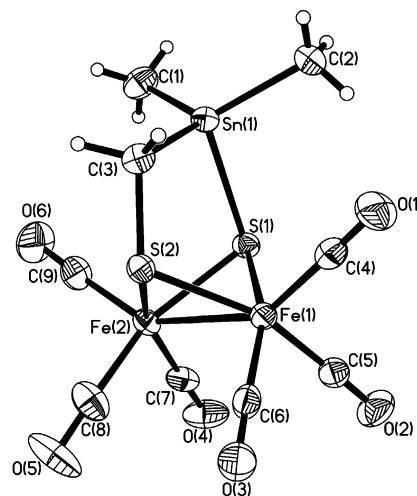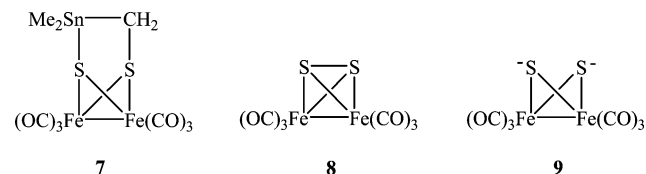
**Figure 1.** ORTEP drawing of **7** with atomic numbering and 50% probability ellipsoids.

by X-ray crystallographic analysis, and an ORTEP drawing of this compound is shown in Figure 1. Variable-temperature

7   **8**   **9**

NMR studies have shown[18] that the three-carbon bridge in **3a** inverts rapidly at room temperature but slow exchange is achieved at −80 °C. Analogy has been drawn between this process in a fused iron−dithiocyclohexane and chair-to-chair ring inversion in cyclohexane. The $\Delta G^{\ddagger}$ calculated for this barrier in **5**, that is, inverting the $CH_2SnMe_2CH_2$ bridge, is 1.23 kcal/mol, and no temperature dependence in the NMR spectra of **5** was observed experimentally. This lower barrier for ring inversion for **5** than **3a** is consistent with the reported[19] lowering of the ring inversion barrier in cyclohexane on replacing a ring carbon with silicon.

Alkylation of dithiolate **9** with Me_3SnCH_2I[14,20] provided a mixture of dialkylated products in 49% yield. Similarly, methylation of **9** with iodomethane yields a mixture of e,e and a,e-dimethylated products.[14] The e,e-isomer, **10**, and a,e-

10   **11**

12
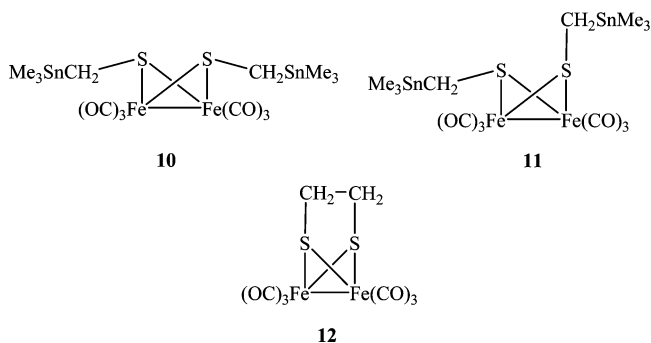
isomer, **11**, can be separated by chromatography on silica gel, and are readily distinguished by ^1H NMR spectroscopic

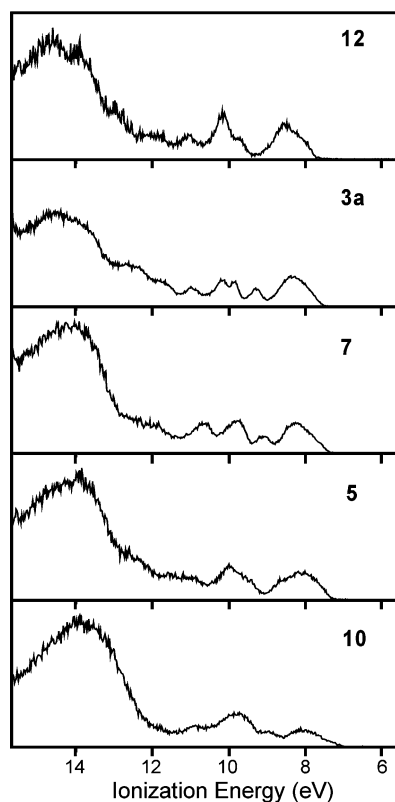**Figure 2.** Gas-phase photoelectron spectra of **12**, **3a**, **7**, **5**, and **10**.

Figure 3. Comparison of He I and He II spectra of **12**, **3a**, **7**, **5**, and **10**.

Table 1. Fit Parameters for Photoelectron Spectra of **12**, **3a**, **7**, **5**, and **10**[a]

		relative area		
gaussian	position(s)	He I	He II/ He I	label
12 (onset = 7.71 eV)				
1	7.98	1	1	Fe−Fe bent σ
2−4	8.24−8.94	5.52	2.13	Fe 3d
5	9.75	2.26	0.17	$S_\perp^-$
6,7	10.14, 11.08	6.77	0.35	S 3p
3a (onset = 7.53 eV)				
1	7.86	1	1	Fe−Fe bent σ
2−4	8.12−8.75	4.72	2.41	Fe 3d
5	9.32	1.57	0.54	$S_\perp^-$
6−8	9.54−10.98	6.62	1.18	S 3p
7 (onset = 7.32 eV)				
1	7.65	1	1	Fe−Fe bent σ
2−4	7.95−8.61	5.88	2.32	Fe3 d
5	9.08	1.86	0.31	$S_\perp^-$
6−11	9.63−11.02	10.07	1.87	S 3p, Sn−C σ
5 (onset = 7.23 eV)				
1	7.61	1	1	Fe−Fe bent σ
2−4	7.93−8.51	3.79	4.74	Fe 3d
5	8.08	0.64	0.45	$S_\perp^-$
6−13	9.11−11.21	7.88	7.41	S 3p, Sn−C σ
10 (onset = 7.04 eV)				
1	6.38	1	1	Fe−Fe bent σ
2−4	7.83−8.47	5.33	2.96	Fe 3d
5−14	8.84−12.04	25.97	3.94	S 3p, Sn−C σ

[a] All energies in eV.

analysis. Isomer **10** shows two singlets in a 9:2 ratio, whereas **11** exhibits four singlets in a 9:9:2:2 ratio. Samples of the known compounds **3a**[16a] and **12**[16b,21] were also synthesized for spectroscopic comparison with their tin analogues.

Photoelectron Spectroscopy. The gas-phase photoelectron spectra collected with a He I photon source in the energy region from 6 to 15 eV for **12**, **3a**, **7**, **5**, and **10** are shown in Figure 2. The comparison shown in this figure emphasizes that the electronic structure and hence the subsequent photoelectron spectra of these molecules are very similar, but distinct differences are observed in the lower ionization energy region below about 12 eV. Spectra of each of these complexes collected with both He I and He II photon sources and focusing on this ionization energy region below 12 eV are shown in Figure 3.

In Figure 3, the experimental data are modeled analytically with asymmetric Gaussians peaks with parameters given in Table 1. It is important to note that, due to the complex electronic structure of these molecules, the Gaussians used to model the shape of the spectral features are not able to be assigned to represent individual ion states. Rather, the deconvolutions allow for quantitative comparisons of the ionization band structure. It is important to stress that many features that provide for qualitative comparisons for these
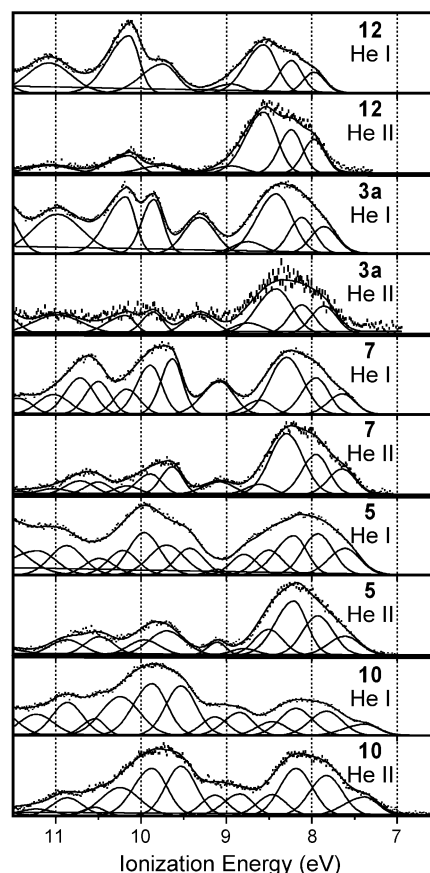
molecules are clearly visually apparent for the spectra. For each of these molecules, ionizations will be observed in the ionization energy region below 12 eV that correspond to

(17) Seyferth, D.; Vic, S. C. *Synth. React. Inorg. Metal-Org. Chem.* **1974**, *4*, 515.
(18) Lyon, E. J.; Georgakaki, I. P.; Reibenspies, J. H.; Darensbourg, M. Y. *J. Am Chem. Soc.* **2001**, *123*, 3268−3278.
(19) Arnason, I.; Kvaran, A.; Jonsdottrir, S.; Gudnason, P. I.; Oberhammer, H. *J. Org. Chem.* **2002**, *67*, 3827−3831.
(20) Seyferth, D.; Andrews, S. B. *J. Organomet. Chem.* **1969**, *18*, P21.
(21) King, R. B. *J. Am. Chem. Soc.* **1963**, *85*, 1584.

removal of an electron from (a) the Fe−Fe σ bond orbital that is formed by the contribution of one electron from each of the Fe(I) d^7 metal centers, (b) the primarily 3d Fe-based orbitals that are occupied by the remaining 12 electrons from the two Fe(I) centers, (c) the Fe−S σ bond orbitals, and (d) the S 3p lone pair orbitals. Also, the Sn-containing molecules will have additional ionizations from Sn−C σ bonds in this region. The general assignment of the spectral features of these molecules is based on comparison to previous work on related molecules, by comparison to trends observed within the series of molecules studied here, and by comparison of the spectra of each molecule collected with He I and He II photon sources. The comparison of He I and He II data gives insight into the atomic character of the orbitals that are associated with particular ionization bands because ionizations from predominantly Fe 3d-based orbitals will be expected to increase in relative area in the He II spectra compared to predominantly p-block-based orbitals, as has observed for many other molecules and as predicted by theoretical calculations of atomic photoionization cross-sections. For the most part, the general assignments given are also supported by the electronic structure calculations also carried out as part of this study. The following discussion first considers how the photoelectron spectra can be assigned on the basis of only empirical evidence, and the subsequent section presents results from DFT calculations that are compared with the empirical assignments.

First, we will consider the photoelectron spectra of **12** and build from the spectra of this molecule to consider the spectra of the other molecules presented. The assignment of the general character of the ionizations of **12** is aided by comparison to the previously reported spectra of related compounds.[22−24] For example, similar to the spectrum of **12**, the spectra of $(\mu\text{-}S_2)[Fe(CO)_3]_2$[22,23] and the anti (e,e) isomer of $(\mu\text{-}iso\text{-}C_3H_7S)_2[Fe(CO)_3]_2$[23] contain a broad featureless band of ionizations between about 8 and 9 eV that has been assigned to the ionizations from the Fe 3d orbitals, with a discernible shoulder on the low-ionization-energy side assigned to the ionization from the fairly weak, "bent" Fe−Fe bond orbital.[23] The spectra of the previously studied neutral molecules also contain a second band between about 9 and 11 eV that was assigned to ionization from orbitals that are primarily sulfur 3p in character. In comparison, the energy region from about 9 to 12 eV in the spectra of **12** contains somewhat better-resolved band features so that a 1:2:1 pattern can be observed. All of the bands from 9 to 12 eV decrease substantially in relative intensity compared to the band from 8 to 9 eV on going from the He I to He II spectrum, in agreement with an assignment of the ionizations from 8 to 9 to predominantly iron-based orbitals and the ionizations from 9 to 12 eV to predominantly sulfur-based orbitals. The spectra illustrate the large intensity differences that are observed for primarily Fe 3d- and S 3p-based ionizations;

clearly, if there were a sulfur-based ionization in the same energy region as the metal-based ionizations, much greater differences would be observed in the 8−9 eV band profile.

The analytical fit of the 8−9 eV band for **12** requires four Gaussians to adequately represent its shape, and it is not possible to fully assign vertical ionization energies for the seven total ionizations expected in this region. However, similar to the spectra of the previously studied Fe_2S_2 compounds, there is a discernible shoulder on the low-energy side of this band that is modeled with the lowest-energy Gaussian band. This Gaussian holds its intensity more than the other Gaussians in the He II spectra, indicating that it represents an orbital or orbitals with a higher percentage of iron character than the other orbitals under this band. In agreement with the assignment of the iron dimers previously reported, this Gaussian is assigned to primarily represent the Fe−Fe bond orbital.

As will be illustrated further in the discussion of the computational results, the bridging nature of the dithiolate ligand of **12** will cause a strong repulsive interaction in the antisymmetric combination of sulfur 3p orbitals that are aligned perpendicular to the Fe−Fe vector, along the S−S vector. This interaction will result in an orbital that will be denoted as $S_\perp^-$. This orbital is expected to lead to the lowest-energy sulfur-based ionization, and therefore, the Guassian at 9.75 eV is assigned to primarily represent $S_\perp^-$ for **12**.

The spectra of **3a** shown in Figure 3 are very similar to those of **12**. The center band of the 1:2:1 pattern observed for **12** is now somewhat separated in energy from the other bands. In general, all of the ionizations are somewhat destabilized from the positions of the ionizations of **12**. For example, the Gaussian that represents the first sulfur-based ionization is now at 9.32 eV.

The main difference between the photoelectron spectra of the stannylated iron dithiolates that also have bridging ligands, **5** and **7**, and those of their carbon-bridged analogues, **12** and **3a**, is the presence of additional ionizations between about 9.5 and 12 eV due to Sn−C σ bond ionizations. The fact that these ionizations are in the same energy range as the S 3p ionizations is an indication of the interactions that will be likely between Sn−C σ and S 3p orbitals. Note also that the Gaussian that represents the first sulfur-based ionization of **7** is now destabilized to 9.08 eV. For **5**, this ionization is destabilized to such an extent that is now falls under the same band as the predominantly metal-based ionizations, as evidenced by the distinct change in band profile in the He II spectrum, especially at the high-energy edge of the first band. As compared to the previously described spectra, which all required four Gaussians to describe the shape of the metal band, an additional fifth Gaussian at 8.80 is now required to properly model the shape of this band for **5**. Since this Gaussian shows a dramatic reduction in relative intensity from the He I to He II spectra as compared to the other Gaussians used to fit this band, this fifth Gaussian is assigned to the $S_\perp^-$ orbital ionization.

The sample that was used to collect the spectra of **10** shown in Figure 3 was the e,e-isomer, but it is possible that other isomers are also present in the gas phase at the

(22) Anderson, E. L.; Fehlner, T. P.; Foti, A. E.; Salahub, D. R. *J. Am. Chem. Soc.* **1980**, *102*, 7422−7429.
(23) Van Dam, H.; Louwen, J. N.; Oskam, A.; Doran, M.; Hillier, I. H. *J. Electron Spectrosc. Relat. Phenom.* **1980**, *21*, 57−69.
(24) Yang, X.; Razavet, M.; Wang, X.-B.; Pickett, C. J.; Wang, L.-S. *J. Phys. Chem. A* **2003**, *107*, 4612−4618.
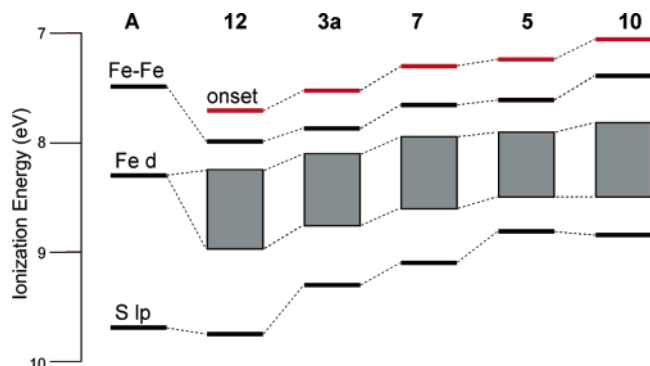
Figure 4. Correlation diagram comparing selected ionization energies for $(\mu\text{-}iso\text{-}C_3H_7S)_2[Fe(CO)_3]_2$ (**A**), **12**, **3a**, **7**, **5**, and **10**.

temperatures required to sublime the sample. Even with the possibilities of multiple isomers, the spectra of **10** are still mostly similar to those of the other compounds discussed to this point, although the region of the spectra higher than about 9 eV are more complicated. The lowest-energy Gaussian that appears to represent ionization(s) with primarily sulfur 3p or Sn−C bond character is located at 8.84 eV. It is important to note that the e,e-isomer will not have the strong through-space destabilizing interactions of S lone pair orbitals that will be present for the molecules with bridging dithiolates that are constrained in the a,a structure. The orientation of the S lone pair orbitals and the subsequent interactions possible with the Fe 3d orbitals will be discussed in further detail with the computational results. Note that the shoulder on the low-ionization-energy side of the metal band for **10**, which is again assigned primarily to represent the Fe−Fe σ bond ionization, is now more visually distinct as it has been destabilized away from the other metal-based ionizations.

Trends in Ionization Energies. A correlation diagram that illustrates a comparison of the experimental ionization energies is shown in Figure 4. This diagram compares the ionization energies of the Fe−Fe σ bond, the other metal d orbitals, and the lowest-energy sulfur lone pair-based ionization for $(\mu\text{-}iso\text{-}C_3H_7S)_2[Fe(CO)_3]_2,$[23] **12**, **3a**, **7**, **5**, and **10**. For $(\mu\text{-}iso\text{-}C_3H_7S)_2[Fe(CO)_3]_2$, the positions shown are the values reported as vertical positions by Hillier and co-workers,[23] while for the others, the values shown are taken from the positions of Gaussians used to deconvolute the data. For the metal d ionizations, a gray box is used to indicate the spread of energies between the lowest- and highest-energy Gaussians that model the shape of the metal band. In addition, for the last five complexes, the onset of ionization, as defined in the Experimental Section, is also shown with red lines.

Figure 4 emphasizes the fact that the sulfur lone pair ionization is greatly destabilized for the stannylated complex **7**, as compared to the alkylthiolate complexes **12** and **3a**. The metal ionizations, and particularly the Fe−Fe σ bond also are affected by the increased electron-donor ability of the stannylated ligand and are also significantly destabilized. The destabilization of the sulfur lone pair ionizations of the stannylated molecules is ascribed to the previously identified neighboring tin effect.[25] That is, the energy of the filled C−Sn σ bond in **5** and its alignment with the sulfur lone

pair orbital results in their interaction. In the case of 2,2-bis(trimethylstannyl)-1,3-dithiane, **13a**, this resulted in a

13a, R=Me₃Sn
b, R=H

14
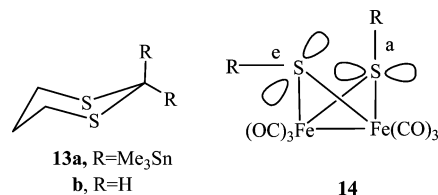
lowering of the sulfur lone pair ionization potential by 1 eV relative to 1,3-dithiiane **13b**. Similarly, the antisymmetric sulfur lone pair orbital in **7** is lowered by 0.67 eV (9.75−9.08 eV) compared with its carbon analogue, **12**. In this case, in addition to the C−Sn σ-bond interaction with the sulfur lone pair, there is a Sn−S bond. The electronic effect of R_3Sn on an attached sulfur has been discussed in the literature[26] in terms of inductive, $p_\pi\text{-}d_\pi$ resonance and hyperconjugative effects. The inductive and hyperconjugative effects increase electron density on sulfur, but $p_\pi\text{-}d_\pi$ resonance decreases it. The consequence of these opposing effects is that the electron density on sulfur in Sn−S compounds and the corresponding C−S compounds are similar. Thus, the S_{2p} ionization energies from ESCA[27] and the S_{3p} ionization energies from mass spectroscopic[28] and photoelectron spectroscopic measurements are comparable.[28]

The correlation diagram in Figure 4 also illustrates that spectral differences between the complexes **12**, **3a**, and **7**, which contain bridging μ-dithiolate ligands as opposed to two μ-thiolate ligands for $(\mu\text{-}iso\text{-}C_3H_7S)_2[Fe(CO)_3]_2$ and **10**. An important structural difference between these two types of molecules is the orientation of the 3p sulfur lone pairs with respect to the Fe−Fe bond and, hence, the amount of repulsive interactions between the sulfur lone pairs. The bridging μ-dithiolate ligand is pinned into an a,a orientation with the sulfur lone pair orbitals perpendicular to the Fe−Fe σ bond, while the preferential orientation of two μ-thiolate ligands gives the e,e isomer with the sulfur lone pair orbitals oriented in such a way that filled−filled interaction with the Fe−Fe σ bond is possible (see **14** for illustration of the difference in S lone pair orientation for a- and e-substituents). The strength of the S lone pair Fe−Fe σ bond interaction in the e,e isomer is evidenced by the low ionization energies of the Fe−Fe σ bond for $(\mu\text{-}iso\text{-}C_3H_7S)_2[Fe(CO)_3]_2$ and **10**. The computational results presented in the next section will also give further evidence of this geometric dependence of sulfur lone pair with Fe−Fe σ bond overlap.

Computational Studies

In general, the results of the hybrid density functional computational studies are in agreement with the general descriptions of electronic structure and the trends observed

(25) Glass, R. S.; Radspinner, A. M.; Singh, W. P. *J. Am. Chem. Soc.* **1992**, *114*, 4921−4923.
(26) Pirrazzini, G.; Danieli, R.; Ricci, A.; Boicelli, C. A. *J. Chem. Soc., Perkin Trans. 2* **1974**, 853−856, and references therein.
(27) Pignataro, S.; Lunazzi, L.; Boicelli, C. A.; Di Marino, P.; Ricci, A.; Mangini, A.; Danieli, R. *Tetrahedron Lett.* **1972**, 5341−5344.
(28) Distefano, G.; Ricci, A.; Danieli, R.; Foffani, A.; Innorta, G.; Torroni, S. *J. Organomet. Chem.* **1974**, *65*, 205−208.

Table 2. Calculated Ionization Energies, Orbital Energies, and Orbital Characters for **12**, **3a**, **7**, **5**, **10**, and **11**[a]

	12		3a		7		5		10		11	
orbital	energy (eV)	principal character	energy (eV)	principal character	energy (eV)	principal character	energy (eV)	principal character	energy (eV)	principal character	energy (eV)	principal character
HOMO	8.25	Fe−Fe σ	8.10	Fe−Fe σ	7.99	Fe−Fe σ	7.76	Fe−Fe σ	7.61	Fe−Fe σ	7.79	Fe−Fe σ
HOMO-1	8.99	S lp	8.58	S lp	8.59	S lp	8.27	S lp	8.32	S lp	8.27	S lp
HOMO-2	9.05	Fe 3d	8.84	S lp	8.77	Fe 3d	8.53	S lp	8.48	S lp	8.66	S lp
HOMO-3	9.23	Fe 3d	9.06	S lp	8.85	S lp	8.69	S lp	8.60	S lp	8.66	S lp
HOMO-4	9.27	S lp	9.14	Fe 3d	9.06	Fe 3d	8.93	Fe 3d	8.66	S lp	8.88	S lp
HOMO-5	9.67	Fe 3d	9.37	Fe 3d	9.34	Fe 3d	9.06	S lp	9.00	Fe 3d		
HOMO-6	9.68	Fe 3d	9.43	Fe 3d	9.73	S lp	9.06	Fe 3d	9.03	Fe 3d		
HOMO-7	10.04	S lp	9.84	S lp	9.97	S lp	9.08	Fe 3d	9.35	Fe 3d		
HOMO-8	10.18	S lp	10.00	S lp	10.43	S lp	9.42	Fe 3d				
HOMO-9	11.30	S lp	10.02	S lp			9.69	S lp				

[a] See the Experimental Section for further details on how the calculations were performed.

experimentally by photoelectron spectroscopy, and also give additional insight into the character of the orbitals and the nature and importance of the symmetry-allowed orbital interactions that have been described to this point. The calculated first vertical ionization energies of compounds **3a**, **5**, **7**, and **10**−**12** are given in Table 2, along with corrected Koopman's theorem orbital ionization energies for the top few orbitals. The trends in the calculated energies of the Fe− Fe bent σ bond, which is calculated to be the HOMO for each of these compounds, and the orbitals containing significant sulfur 3p character agree with the experimental trends. There are some differences between the experimental and computational results; for example the computational results consistently give higher ionization energies for the metal-based orbitals compared with the photoelectron spectroscopic results, while the opposite is true for the sulfur-based orbitals. The computational results for each of these molecules place the sulfur orbital with lowest ionization energy lower than the Fe d orbital ionizations (albeit higher in energy than the HOMO Fe−Fe σ-bond ionization energy) in contrast to the experimental results. As discussed earlier, the comparison of the He I and He II spectra of each of these molecules clearly shows that there is no orbital with predominantly sulfur character in the same energy region as the Fe d orbital ionizations.

Further discussion of the computational results will begin by considering the calculated orbitals of **3a** as a starting point and will then evaluate the perturbations to these orbitals caused by lowering of symmetry, stannylation, and geometry differences. Orbital plots of the first five occupied frontier orbitals of **3a** are shown in Figure 5 (the next six occupied orbitals are shown in the Supporting Information). The orbitals of **12**, which are not shown, are virtually identical to those of **3a**, as would be expected for these closely related alkylthiolates. In agreement with the description of the experimental results, these calculations show the HOMO of **3a** to be the "bent" Fe−Fe σ bond. However, the calculated relative orbital energies as shown in Table 2 do not agree well with the pattern of ionization bands observed in the experimental spectra, and the orbital plots show that the theoretical results are placing predominantly sulfur-based orbital between the HOMO and the other predominantly metal-based orbitals. Because of the similar calculated energies of the Fe d orbitals and sulfur lone pair orbitals
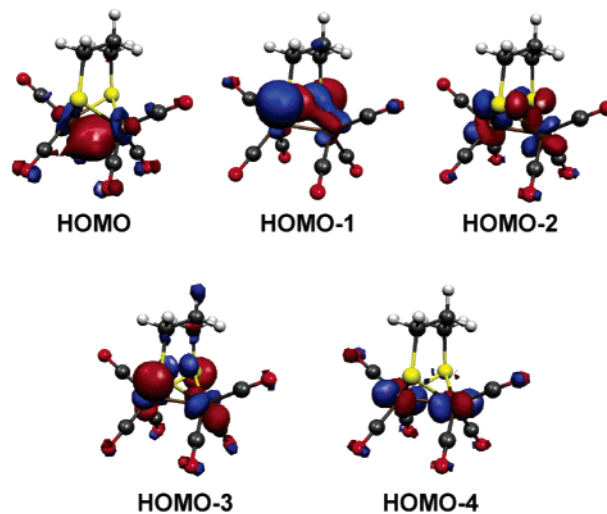

Figure 5. Orbital surfaces (value = ±0.05) for frontier orbitals of **3a**.

and the many possibilities for symmetry matching, there is a high degree of mixing of Fe d orbital and sulfur lone pair orbital character in all of the calculated frontier valence orbitals. This is in contrast to the experimental results because the comparison of the He I and He II spectra of **3a** clearly shows a distinct difference in Fe 3d versus sulfur 3p atomic character for the orbitals from which the valence ionizations originate. There is of course mixing of character, but the calculations are overemphasizing the degree of this mixing because they are placing the Fe and S orbitals too close in energy.

Even though the calculations do not properly predict the relative order of the ionizations of **3a**, the orbitals do illustrate the symmetry features expected. For example, the HOMO-1 of **3a** shown in Figure 5 contains the principal character from the orbital labeled $S_{\perp}^{-}$ for the experimental results on the complexes with a bridging dithiolate ligand (the HOMO-7 also contains character from this orbital). The HOMO-3 and HOMO-10 of **3a** also contain character from sulfur lone pairs perpendicular to the Fe−S−Fe planes, while the HOMO-2, HOMO-8, and HOMO-9 contain character from sulfur lone pairs in the Fe−S−Fe planes.

As found experimentally, the computational results also show that the sulfur lone pair orbitals are destabilized for the stannylated complexes as compared to the alkylthiolate complexes. For example, it is found computationally that

the lowest-energy sulfur lone pair (HOMO-1) of **7** is destabilized by 0.40 eV from that of **12**, while the comparable experimental ionization of **7** is destabilized by 0.67 eV from that of **12**. For compound **12**, the HOMO-1 is again the $S_\perp^-$ lone pair orbital, which looks virtually identical to the HOMO-1 of **3a** shown in Figure 5. There are also perpendicular sulfur-type orbitals calculated for the stannyl analogue **7**, but the lowering of symmetry by stannylation of one of the sulfurs splits the $S_\perp^-$ lone pair orbital into the two more localized orbitals **15** (HOMO-1) and **16** (HOMO-3). The

15   **16**
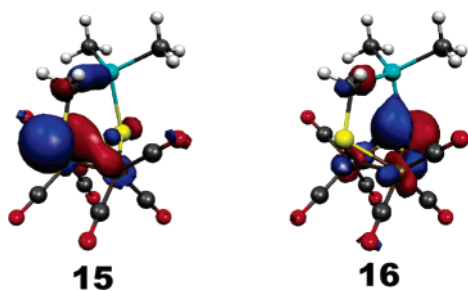
HOMO-1 (**15**) is now a lone pair predominantly localized on the sulfur bonded to carbon. The orbital plot shown in **15** also illustrates that this lone pair orbital has a destabilizing, filled−filled interaction with the Sn−C σ bond; this orbital is destabilized 0.14 eV from the corresponding orbital in **12**. The lone pair localized on the sulfur that is directly bonded to the electropositive tin (**16**) occurs 0.27 eV below the other sulfur lone pair. The calculations show that the HOMO-1 of **3a** and **5** are related but the HOMO-1 of **5**, as shown in **17**, is now destabilized by interaction with two

17
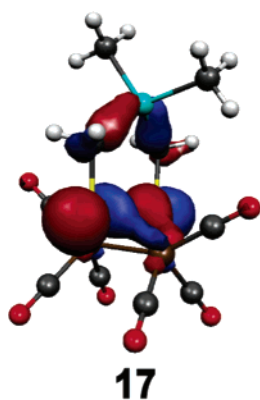
C−Sn σ bonds. The substantial destabilization of the Fe−Fe σ-bond ionization observed experimentally on stannylation (0.33 eV lowering for **7** compared with **12**) is also found computationally (0.27 eV).

The predominantly sulfur-based orbitals for **10** and its a,e-isomer **11** (see Supplementary Information) are different from those of **3a** or **5**. As can be seen in Table 2, the calculated sulfur lone pair orbital energies of **10** have also been destabilized from the energies of the comparable orbitals of **3a** upon stannylation. For **10**, the sulfur lone pair orbitals have mixed to form a set of four orbitals that are shown in Figure 6. Two of these orbitals (HOMO-3 and HOMO-4) are oriented parallel to the Fe−Fe σ bond and are similar to lone pair orbitals of the bridging dithiolate systems; for
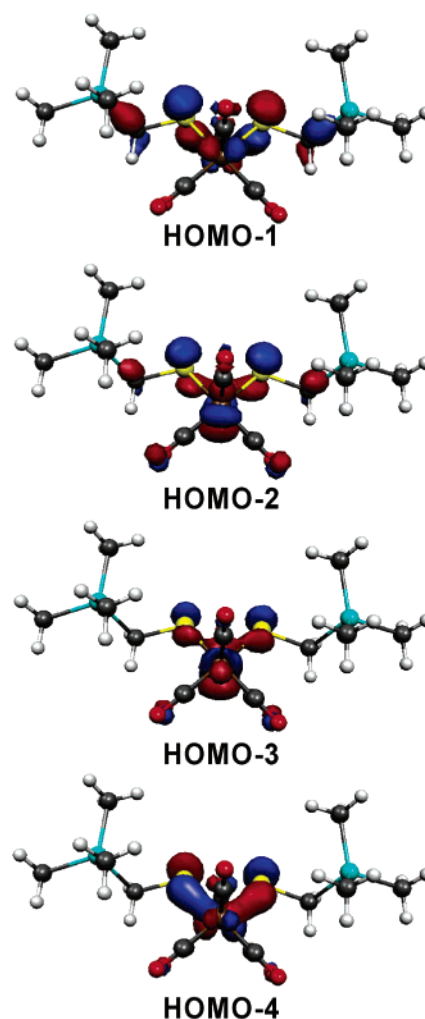
Figure 6. Orbital surfaces (value = ±0.05) for the predominantly sulfur lone pair orbitals of **10**.

example, the HOMO-3 of **10** shown in Figure 6 is analogous to the HOMO-2 of **3a** shown in Figure 5. The other two sulfur lone pair orbitals of **10** (HOMO-1 and HOMO-2), however, are very different from the other set of sulfur lone pair orbitals of **3a**. These two orbitals of **10** have electron density in the S−Fe−S plane and also contain character from C−Sn σ bonds and most importantly have a much different orientation with respect to the Fe−Fe σ bond than any sulfur lone pair orbitals for the bridging dithiolate molecules.

The calculations show that the presence of a vicinal C−Sn σ bond does destabilize the Fe−Fe σ bond orbital, but similar to the experimental ionization-energy trends, indicate that the extent of this effect is geometry dependent. A consideration of the orbital plots for the sulfur lone pair orbitals of the bridging versus the nonbridging systems gives insight into this geometry dependence, as the HOMO-2 of **10** would be expected to have good overlap with the Fe−Fe σ bond orbital, and indeed, some metal character is present in this orbital. A comparison of the HOMOs of **5**, **10**, and **11** are shown in Figure 7, with views of each orbital shown both down the sulfur−sulfur vector and down the iron−iron vector. For **5**, where both sulfurs are axially substituted, the sulfur lone pairs are oriented in such a way that there is no contribution from the sulfur lone pairs to the HOMO.
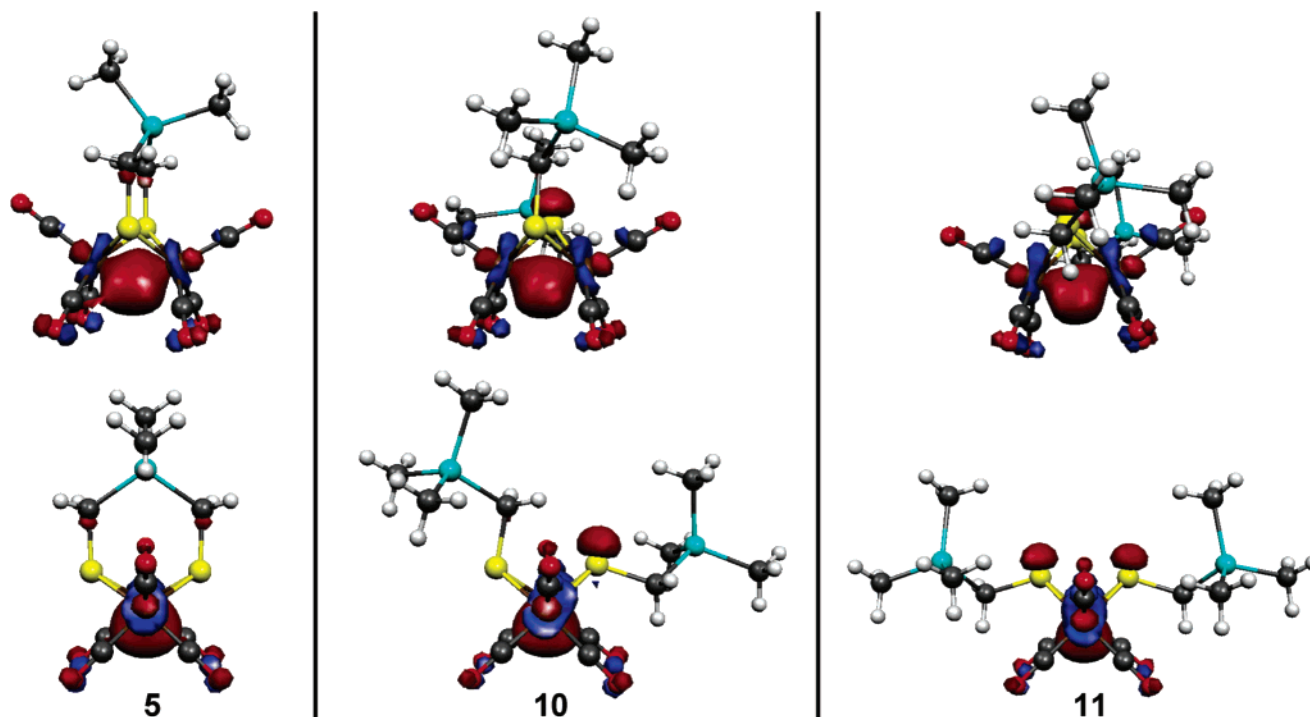
Figure 7. Orbitals surfaces (value = ±0.05) for the HOMOs of **5**, **10**, and **11**.

However, for both **10** and **11**, the HOMO contains a distinct contribution from the equatorially substituted sulfur atom lone pair(s).

Conclusions

In summary, the orbital assignments obtained by PES and computational methods for **12**, **3a**, **7**, **5**, and **10** are analogous to those reported before for other dinuclear iron dithiolates but with the anticipated destabilization of sulfur lone pair orbitals by C−Sn bonds. In addition, there is a significant destabilization of the metal-based ionizations, in particular the Fe−Fe σ bond that is believed to be a reactive site in this class of molecules. Unfortunately, photoelectron spectra have not yet been reported for the phosphine-substituted iron dithiolates reported by others to allow comparison of the donor effects of the stannylated dithiolates to those of phosphines. There are two important but distinct geometry-dependent ways by which the ionization energy of the Fe−Fe σ bond is lowered upon stannylation of the thiolates. The first involves direct mixing of a lone pair orbital on sulfur with the Fe−Fe σ bond if the thiolate substituent is in an equatorial position, the preferred orientation for nonbridging thiolates. The second involves increased electron donation from sulfur to the metal center, which is induced by C−Sn σ-bond interaction with the sulfur lone pair, but does not involve direct mixing of the sulfur lone pair orbital and Fe−Fe σ-bond. The destabilization of the Fe−Fe bond by a sulfur lone pair with appropriate geometry may be important in the catalytic mechanism of [Fe] hydrogenase. Specifically, the nonbridging sulfur in **2** that is attached to one iron may weaken the Fe−Fe bond and, since it is attached to one iron, promote unsymmetrical cleavage of this bond, a process already suggested as a key mechanistic step.

Experimental Section

General Methods. ^{1}H and ^{13}C NMR spectra were obtained using a Varian Unity 300 instrument at 299.954 MHz for ^{1}H and 75.431 MHz for [13]C. Chemical shifts are reported relative to CDCl$_3$ (7.24 and 77.0 ppm for ^{1}H and ^{13}C, respectively). IR spectra were recorded on a Nicolet Impact 410 spectrophotometer. FAB-MS data were obtained using a Finnigan MAT-95 spectrometer. Elemental analyses were determined by Desert Analytics, Tucson, AZ. Melting points were determined using a Buchi capillary melting point apparatus and are uncorrected. THF was freshly distilled from sodium−benzophenone ketyl under nitrogen. Silica gel (230−400 mesh), purchased from Natland International Corp., was used for column chromatography eluting with *n*-hexane. All other reagents were obtained from Aldrich Chemical Co., Milwaukee, WI. All reactions were carried out under nitrogen using standard Schlenk line techniques.

Synthesis of [(μ-Me$_3$SnCH$_2$S)Fe(CO)$_3$]$_2$ (10, 11). Following the procedure of Seyferth et al.,[16,20] a solution of dianion **9** was prepared as follows. A solution of (μ-S)[Fe(CO)$_3$]$_2$, (**8**),[15] (100 mg, 0.29 mmol) in anhydrous THF (5 mL) under a nitrogen atmosphere was cooled to −78 °C. A solution of 1 M LiEt$_3$BH in THF (0.62 mL, 0.62 mmol) was added dropwise over 30 min. To this emerald green solution was added a solution of Me$_3$SnCH$_2$I[14,20] (265 mg, 0.87 mmol) in THF (1 mL) at −78 °C. The mixture was stirred at this temperature for 1 h, allowed to warm to room temperature, and stirred for 2 h. The now dark-red solution was concentrated and chromatographed (hexane) to give a mixture of **10** and **11** (99 mg, 49% yield): IR (CHCl$_3$) 2062, 2022, 1990 cm^{-1}; ^{1}H NMR δ 0.18 (s, CH$_2$), 0.25 (s, CH$_3$), 0.28 (s, CH$_3$), 1.53 (s,CH$_2$), 1.91 (s,CH$_3$), 1.99 (s, CH$_2$); ^{13}C NMR δ −9.2 (CH$_3$), −9.0 (CH$_3$), 18.0 (CH$_2$), 20.0 (CH$_2$), 209.3 (CO), 210.3 (CO); FAB HRMS *m/z* Calcd for C$_{14}$H$_{22}$O$_6$Fe$_2$S$_2$Sn$_2$: 699.7604. Found: 699.7654. The isomers could be separated on rechromatography. **10**: ^{1}H NMR δ 0.23 (s,CH$_3$) 1.91 (s,CH$_2$). **8**: ^{1}H NMR δ 0.18(s, CH$_3$), 0.28(s, CH$_3$), 1.53 (s, CH$_2$), 1.99 (s, CH$_2$).

Table 3. Crystal Data[a] for **7**

mol formula	$C_9H_8Fe_2O_6S_2Sn$
mol wt	506.66
space group	$C2/c$ (no. 15)
a, Å	24.876(3)
b, Å	10.0882 (10)
c, Å	14.7933 (15)
α, deg	90
β, deg	121.726 (2)
γ, deg	90
Z	8
d_{calc}, g cm^{-3}	2.132
cryst color, shape	orange-red plate
cryst dimens, mm	$0.05 \times 0.26 \times 0.50$
no. unique data	3248
no. obsd data	2761
abs coeff[$\mu (\lambda)$], mm^{-1}	3.663

[a] Standard deviation of the least significant figure is given in parentheses.

Synthesis of [(μ-SCH$_2$SnMe$_2$CH$_2$S)Fe$_2$(CO)$_6$ (5). A solution of dianion **9** was prepared as described above from (μ-S$_2$)-[Fe(CO)$_3$]$_2$, (**8**), (200 mg, 0.58 mmol) in THF (8 mL), and 1 M LiBEt$_3$H in THF solution (1.3 mL, 1.3 mmol). To this solution at −78 °C was added trifluoroacetic acid (0.10 mL, 1.3 mmol). This solution was stirred at −78 °C for 1 h, warmed to room temperature, and stirred for an additional 0.5 h. A solution of Me$_2$(SnCH$_2$I)$_2$[14] (412 mg, 0.96 mmol) in THF (5 mL) was added followed by triethylamine (0.38 mL, 2.7 mmol) in portions over 10 min. The solution was stirred for 1 h after completion of the addition then concentrated and chromatographed to give **5** as a red solid (39 mg, 13% yield): IR 2063, 2031, 1991, 1974 cm^{-1}; ^{1}H NMR δ 0.25 (s, 3H, CH$_3$), 1.79 (s, 2H, CH$_2$); ^{13}C NMR δ −7.1, 1.6, 207.0; FAB HRMS Calcd for C$_{10}$H$_{11}$O$_6$S$_2$Fe$_2$Sn: 522.7718. Found: 522.7696.

Synthesis of (μ-SSnMe$_2$CH$_2$S)Fe$_2$(CO)$_6$ (7). To a solution of dianion **9** prepared as described above for the synthesis of **10** and **11**, was added Me$_2$Sn(I)CH$_2$I[17] (125 mg, 0.30 mmol) in THF (1.5 mL) at −78 °C. The solution was stirred at −78 °C for 1 h, warmed to room temperature and stirred an additional 2 h, and then concentrated and chromatographed to give **7** as a dark-red solid (45 mg, 30% yield): IR (CDCl$_3$) 2071, 2023, 2007, 1966 cm^{-1}; ^{1}H NMR δ 0.59 (s, 6H, CH$_3$), 1.88 (s, 2H, CH$_2$); ^{13}C NMR δ −3.3, 17.7, 208.4; MS: 507, 505. Anal. Calcd for C$_9$H$_8$O$_6$S$_2$SnFe$_2$: C, 21.31; H, 1.58. Found C, 21.71; H, 1.67.

X-Ray Single-Crystal Structure Study of 7. An orange-red platelike crystal ($0.05 \times 0.26 \times 0.50$ mm) was mounted on a glass fiber in a random orientation. Examination of the crystal on a Bruker SMART 1000CCD detector X-ray diffractometer at 173 (2) K and a power setting of 50 kV, 40 mA showed measurable diffraction to at least $\Theta = 25.98°$. Data were collected on the SMART 1000 system[29] using graphite-monochromated Mo Kα radiation ($\lambda = 0.71073$ Å). Cell constants and an orientation matrix were determined from reflections obtained in three orthogonal 5° wedges of reciprocal space. A total of 3736 frames at one detector setting covering 0 to 60° 2θ were collected having an exposure time of 10 s. The frames were integrated using the Bruker SAINT software package's[30] narrow frame algorithm. A total of 17 681 reflections were integrated and retained. The final monoclinic cell and other parameters are listed in Table 3 and are based on the refinement of the XYZ centroids of 4124 reflections with $I > 3\sigma (I)$ covering the range $2.24° < \Theta < 25.98°$. Empirical absorption and decay corrections were applied using the program SADABSv2.05.[31]

The structure was solved using SHELXS in the Bruker SHELX-TL (Version 5.0) software package.[32] Refinements were performed using SHELXL, and illustrations were made using XP. Solution of the structure was achieved using direct methods followed by Fourier synthesis. Hydrogen atoms were added at idealized positions, constrained to ride on the atom to which they are bonded and given thermal parameters equal to $1.2-1.5\times$ U$_{iso}$ of that bonded atom. The final anisotropic full-matrix least squares refinement based on F^2 of all reflections converged (max shift/esd = 0.000) at $R_1 = 0.0380$, w$R_2 = 0.0564$, and GOF = 1.040. Conventional refinement indices using the 2761 reflections with $F > 4\sigma(F)$ are $R_1 = 0.0274$, w$R_2 = 0.0537$. The model consisted of 213 variable parameters and no constraints and restraints. There were 24 correlation coefficients greater than 0.50. The highest peak on the final difference map was 0.639 e/Å^3 located 1.03 Å from Sn. The lowest peak on the final difference map was −0.449 e/Å^3 located 1.83 Å from O3. Scattering factors and anomalous dispersion were taken from International Tables, Vol. C, Tables 4.2.6.8 and 6.1.1.4.

Photoelectron Spectroscopy. Photoelectron spectra were recorded using an instrument that features a 36-cm hemispherical analyzer[33] and custom-designed photon source, sample cells, and detection and control electronics.[34] The excitation source is a quartz capillary discharge lamp with the ability, depending on operating conditions, to produce He I (21.218 eV), or He II (40.814 eV) photons. The ionization-energy scale was calibrated using the $^2P_{3/2}$ ionization of argon (15.759 eV) and the $^2E_{1/2}$ ionization of methyl iodide (9.538 eV). The argon $^2P_{3/2}$ ionization also was used as an internal calibration lock of the absolute ionization energy to control spectrometer drift throughout data collection. During He I and He II data collection, the instrument resolution, measured using the full-width-at-half-maximum of the argon $^2P_{3/2}$ ionization, was 0.020−0.030 eV. All of the spectra were corrected for the presence of ionizations caused by other emission lines from the discharge source.[35] The He I spectra were corrected for the He Iβ line (1.866 eV higher in energy and 3% the intensity of the He Iα line), and the He II spectra were corrected for the He IIβ line (7.568 eV higher in energy and 12% the intensity of the He IIα line). All data also were intensity corrected with an experimentally determined instrument analyzer sensitivity function that assumes a linear dependence of analyzer transmission (intensity) to the kinetic energy of the electrons within the energy range of these experiments. The samples all sublimed cleanly with no visible changes in the spectra during data collection. The sublimation temperatures (in °C, at 10^{-4} Torr) for the complexes were **12**, 30−50; **3a**, 35; **7**, 65−95; **5**, 65−90; and for **10**, 65−95 (temperatures were monitored using a "K"-type thermocouple passed through a vacuum feedthrough and attached directly to the ionization cell).

In the figures of the data, the vertical length of each data mark represents the experimental variance of that point.[36] The valence ionization bands are represented analytically with the best fit of asymmetric Gaussian peaks, as described in more detail elsewhere.[36] The Gaussians are defined with the position, amplitude, half-width

(29) Bruker 1997 SMART Reference Manual Version 5.0, Bruker AXS, Inc.: Madision, WI.

(30) Bruker 1997 SAINT Reference Manual Version 5.0, Bruker AXS, Inc.: Madison, WI.

(31) Sheldrick, G. M. SADABS Reference Manual Version 2.03, Bruker AXS, Inc.: Madison, WI, 2000.

(32) Bruker 1997 SHELXTL. Reference Manual Version 5.0, Bruker AXS, Inc.: Madison, WI.

(33) Siegbahn, K.; Nordling, C.; Fahlman, A.; Nordberg, R.; Hamrin. *ESCA: Atomic, Molecular and Solid State Structure Studied by Means of Electron Spectroscopy*; Almqvist and Wiksells: Uppsala, 1967.

(34) Lichtenberger, D. L.; Kellogg, G. E.; Kristofzski, J. G.; Page, D.; Turner, S.; Klinger, G.; Lorenzen. J. *Rev. Sci. Instrum.* **1986**, *57*, 2366.

(35) Turner, D. W.; Baker, C.; Baker, A. D.; Brundle, C. R. *Molecular Photoelectron Spectroscopy*; Wiley-Interscience: London, 1970.

(36) Lichtenberger, D. L.; Copenhaver, A. S. *J. Electron Spectrosc. Relat. Phenom.* **1990**, *50*, 335−352.

for the high-binding-energy side of the peak, and the half-width for the low-binding-energy side of the peak. The peak positions and half-widths are reproducible to about ±0.02 eV ($\approx 3\sigma$ level). The onset of a band is defined as the Gaussian position minus 0.9 times the width to low ionization energy. The accuracy of the ionization onset energy is estimated to be ±0.05 eV. The onset of a band is defined as the Gaussian position minus 0.9 times the width to low ionization energy. The parameters describing an individual Gaussian are less certain when two or more peaks are close in energy and are overlapping. When a region of broad ionization intensity spans numerous overlapping ionization bands, the individual parameters of the Gaussian peaks used to model the total ionization intensity are not characteristic of individual ionization states. Confidence limits for the relative integrated peak areas are about 5%, with the primary source of uncertainty being the determination of the baseline under the peaks. The baseline is caused by electron scattering and is taken to be linear over the small energy range of these spectra. The total area under a series of overlapping peaks is known with the same confidence, but the individual peak areas are less certain.

Computational Methodology. Calculations on the iron–sulfur–tin compounds were made with Gaussian 03 (rev B.04)[37] on two computer systems: a Macintosh G4 2 × 1.25 GHz with 2 GB of RAM (Mac OS 10.2.8) and the NCSA (University of Illinois, Urbana-Champaign site) p690 symmetric multiprocessor system (1.3 GHz processors, 16 w/32 GB of RAM, 7 w/64 GB of RAM, and 4 w/256 GB of RAM; AIX 5.1 operating system).

All computations were carried out using Becke's 3-parameter hybrid method with Perdew and Wang's exchange-correlation functional (B3PW91), which is the most accurate three-parameter hybrid method for the computation of energies at minima (although the gain in accuracy over B3LYP is quite small).[38] Hybrid DFT has the advantage that it is much more accurate for most computational applications than pure DFT or Hartree–Fock theory (indeed, for some applications such as open-shell geometry optimization and bond dissociation, it is better than MP2),[39] but it is still computationally cost-effective, an especially important consideration given the size of the molecules being computed.

All computations were carried out using the CEP-121G split-valence basis set with effective core potentials. Few basis sets are parametrized for tin, and we find that the newer CEP-121G gives somewhat better results than the LANL2DZ ECP basis set we have previously employed. For **7**, the LANL2DZ computed bond lengths reproduced the heavy-atom X-ray structure with a mean absolute deviation of 2.2% (maximum: 4.7% high for S–C bonds), while CEP-121G displayed a mean absolute deviation of 2.1% (maximum: 5.1% high for S–C bonds). For all heavy-atom bond angles, LANL2DZ displayed a mean absolute deviation of 1.7% (maximum: 5.8% low for Fe–S–Fe); for CEP-121G, 1.5% (maximum: 4.4% low for Fe–S–Fe). Although the differences were small, previously we have received poor results from ionization calculations made with LANL2DZ on sulfur systems (as compared to 6-31+G*),[40] and that observation combined with the geometry results led us to believe that the CEP-121G basis set is slightly superior for our purposes.

Each compound was optimized prior to ionization-potential calculation, and in the case of **5**, a ring inversion conformational analysis was also performed. Vertical ionization potentials were computed by the ΔSCF method (total difference between the cation radical energy at the neutral minimized geometry and the neutral energy at that geometry), but orbital energies were estimated from the orbital eigenvalues (by a modification of Koopmans' theorem; see below); the vertical IPs are therefore expected to be more reliable than the orbital energies. For **3a**, the Koopmans' estimate of the ionization energy of the S_2 antisymmetric lone pair ionization energy was checked using GUESS=ALTER to promote an electron from that orbital to the HOMO; the result was a vertical IP for that orbital of 8.797 eV. The method which was used to estimate most of the orbital energies takes the difference between the HOMO eigenvalue and the orbital eigenvalue and adds this to the computed molecular vertical IP (essentially constituting an offset correction to the normal Koopmans' theorem values). This method yields a sulfur antisymmetric lone pair IP of 8.581 eV for **3a**; the GUESS=ALTER difference between the two orbitals was 0.696 eV, and the Koopmans' theorem difference is 0.480 eV. This seems to imply that Koopmans' method gives IPs which are a bit too low, but the difference was judged insufficient to warrant the computational effort involved, since our primary concern is relative differences. Orbitals were visualized using MOLEKEL 4.3.win32.[41]

Supporting Information Available: Tables with calculated geometric parameters for compounds **3a**, **5**, **7**, **11**, **12**, and **14**; orbital surfaces for HOMO-5 to HOMO-10 for **3a**; orbital surfaces for HOMO-1 to HOMO-4 for **11** (pdf); tables of positional parameters and listings of structure factors for X-ray structure study of compounds **7** (cif). This material is available free of charge via the Internet at http://pubs.acs.org.

IC050526Q

(37) Frisch, M. J.; Trucks, G. W.; Schlegel, H. B.; Scuseria, G. E.; Robb, M. A.; Cheeseman, J. R.; Montgomery, Jr., J. A.; Vreven, T.; Kudin, K. N.; Burant, J. C.; Millam, J. M.; Iyengar, S. S.; Tomasi, J.; Barone, V.; Mennucci, B.; Cossi, M.; Scalmani, G.; Rega, N.; Petersson, G. A.; Nakatsuji, H.; Hada, M.; Ehara, M.; Toyota, K.; Fukuda, R.; Hasegawa, J.; Ishida, M.; Nakajima, T.; Honda, Y.; Kitao, O.; Nakai, H.; Klene, M.; Li, X.; Knox, J. E.; Hratchian, H. P.; Cross, J. B.; Bakken, V.; Adamo, C.; Jaramillo, J.; Gomperts, R.; Stratmann, R. E.; Yazyev, O.; Austin, A. J.; Cammi, R.; Pomelli, C.; Ochterski, J. W.; Ayala, P. Y.; Morokuma, K.; Voth, G. A.; Salvador, P.; Dannenberg, J. J.; Zakrzewski, V. G.; Dapprich, S.; Daniels, A. D.; Strain, M. C.; Farkas, O.; Malick, D. K.; Rabuck, A. D.; Raghavachari, K.; Foresman, J. B.; Ortiz, J. V.; Cui, Q.; Baboul, A. G.; Clifford, S.; Cioslowski, J.; Stefanov, B. B.; Liu, G.; Liashenko, A.; Piskorz, P.; Komaromi, I.; Martin, R. L.; Fox, D. J.; Keith, T.; Al-Laham, M. A.; Peng, C. Y.; Nanayakkara, A.; Challacombe, M.; Gill, P. M. W.; Johnson, B.; Chen, W.; Wong, M. W.; Gonzalez, C.; Pople, J. A. *Gaussian 03*, Revision B.04; Gaussian, Inc., Wallingford CT, 2004.
(38) Becke, A. D. *J. Chem. Phys.* **1993**, *98*, 5648–52.
(39) Jensen, F. *Introduction to Computational Chemistry*; John Wiley and Sons: New York, 1999; Chapter 11, pp 264–295.
(40) Lorance, E. D., Ph.D. Dissertation, University of Arizona, 2000, Chapter 3.
(41) MOLEKEL 4.3, Flükiger, P.; Lüthi, H. P.; Portmann, S.; Weber, J. Swiss Center for Scientific Computing, Manno (Switzerland), 2000– 2002; Portmann S. Lüthi, H. P. MOLEKEL: An Interactive Molecular Graphics Tool. *Chimia* **2000**, *54*, 766–770.